INTERNATIONAL JOURNAL FOR NUMERICAL METHODS IN FLUIDS, VOL. 25, 1–19 (1997)

A BOUNDARY ELEMENT METHOD FOR VISCOUS GRAVITY CURRENTS

S. BETELÚ, J. DIEZ*, L. THOMAS, R. GRATTON AND B. MARINO

Instituto de Física Arroyo Seco, Facultad de Ciencias Exactas, Universidad Nacional del Centro de la Provincia de Buenos Aires, Pinto 399, 7000, Tandil, Argentina

SUMMARY

The viscous gravity spreading of a blob of fluid on a rigid, horizontal, no-slip surface is studied numerically by applying the boundary-element method to the Stokes equation in plane symmetry. The two-dimensional unsteady solution is obtained by solving the biharmonic equation for the streamfunction in a given domain to obtain the velocity field, which is then used to track the contour. The spreading is developed by letting adhere to the rigid boundary any fluid element set in contact with it. A detailed description of the two-dimensional flow near the head of a viscous gravity current shows a typical rolling motion which characterizes the advancing mechanism of the spreading. In particular, we obtain scaling laws for the shape and size of the current head in good agreement with previously reported experimental data. Attention is also paid to the validation of the numerical method.

Int. J. Numer. Meth. Fluids, **25**: 1–19 (1997).

No. of Figures: 14. No. of Tables: 0. No. of References: 27.

KEY WORDS: boundary elements; viscous flow; gravity currents; Stokes; creeping; spreading

1. INTRODUCTION

This work is concerned with the numerical calculation of the spreading of a very viscous fluid over a horizontal no-slip surface (substrate) under the action of gravity g. This current belongs to a wider family of flows known as creeping flows (negligible inertia), which have been the subject of several works,[1–4] mainly in the field of geology, geophysics, industrial engineering and environmental sciences.

From the theoretical point of view, viscous gravity spreadings have been studied mainly under the lubrication approximation,[5–8] but even for quite flat liquid distributions this approximation is inadequate near the front where large slopes are present. Therefore a fully two-dimensional treatment is required to describe the head region, which contains the most attractive physical features of the flow. However, unlike the case of inertial gravity currents (high Reynolds numbers), where several studies have been devoted to describe the flow at the current head,[9–11] no equivalent attention has been paid to the study of the flow at the head of viscous gravity currents. As regards laboratory-scale

* Correspondence to: J. Diez, Instituto de Física Arroyo Seco, Facultad de Ciencias Exactas, Universidad Nacional del Centro de la Provincia de Buenos Aires, Pinto 399, 7000, Tandil, Argentina
Contract grant sponsor: CONICET
Contract grant sponsor: Comisión de Investigaciones Científicas de la Provincia de Buenos Aires
Contract grant sponsor: Universidad Nacional del Centro de la Provincia de Buenos Aires

CCC 0271–2091/97/010001–19 $17.50 *Received September 1995*

experiments,[12] Huppert[6] reported a curling over of the free surface at the front and recently Marino *et al.*[13] determined the shape profile and its evolution. These experiments, concerning the spreading of relatively large fluid volumes ($V > 30$ cm^3) in axial symmetry, revealed the presence of a first stage practically unaffected by the surface tension γ, or pure gravity stage, characterized by a round-like shape of the current head. The size h^* of this configuration decreases as the spreading advances, till it becomes of the order of the capillary length $a = \sqrt{(\gamma/\rho g)}$ (ρ is the density). At that moment the pure gravity stage ends and the flow enters into a second stage characterized by a wedge-like shape of the current head, mainly due to capillarity effects. The present work is addressed to a fully two-dimensional numerical study of the flow during the pure gravity regime, which, according to experimental observations, exhibits interesting features such as the geometrical similarity of the round-like shape of the current head. Besides, this regime is the relevant one for large-scale natural creeping flows such as spreading lava domes, mud flows, etc.[1]

As our interest is mainly centred on the head of the current, a description in plane geometry is well suited for comparison with experiments in axial symmetry. Thus we develop a numerical code based on the boundary element technique, which has proved to be adequate for the biharmonic equation that results from the Stokes equation in plane symmetry. The equations are solved formally by a pair of integral equations involving the, as yet unknown, values of the dependent variables and their normal derivatives on the boundary. The contour is approximated by a polygon, so that the integrals appearing in the formal solution are replaced by sums of integrals, one for each side of the polygon. The basis of the technique has been reviewed by Jaswon and Symm,[14] and since then, several authors have contributed to the subject: Fairweather *et al.*[15] introduced the use of piecewise quadratic polynomial approximations for the solution of the Laplace equation; Kelmanson[16] obtained analytic expressions for the piecewise integration of all the kernel functions and used the method to solve steady problems; Kelmanson[17] and Lu and Chang[18] extended the boundary integral method to problems with non-planar free surfaces.

In steady problems the shape of the contour is usually determined by an iterative procedure, so that the boundary condition on the normal stress is finally satisfied within a prescribed error. This approach has been used, for instance, by Goodwin and Homsy[19] to calculate a quasi-steady approximation of the flow of a viscous fluid down a slope near the contact line. In unsteady flows the free profile does not coincide with a streamline; therefore the boundary conditions at the free surface are more complicated than in steady flows. The idea is to obtain the velocity field corresponding to a given initial boundary (free surfaces plus no-slip surfaces). Then the new contour shape is tracked by moving the grid points (nodes) according to this velocity field and so on. This approach has been used by Kuiken[20] to calculate the evolution of an isolated two-dimensional liquid region under the influence of surface tension alone.

For the purpose of this work we develop an extension of the method for unsteady problems with gravity as the driving force and also with free and no-slip surfaces. The instantaneous velocity field calculated by the code is validated by comparison with an analytical solution for the flow in a corner region determined by a straight rigid boundary and a straight free surface. Furthermore, the ability of the code to give a time evolution is demonstrated by resorting to the reversibility of Stokes flows. A relevant point is the spreading mechanism: we simply assume that any fluid element reaching the substrate remains adhered there. This mechanism is numerically simulated by keeping fixed the position of the successive nodes of the free surface as they reach the substrate and then by considering them as nodes of the no-slip surface. The numerical simulations show that the front advances by a rolling motion of a round-like current head with a characteristic shape decreasing in size. This current head shape agrees quantitatively with measurements[13] as long as its size is larger than a. Moreover, within the above limit the scaling laws for the size obtained from simulations are also in excellent agreement with experiments.

In Sections 2.1 and 2.2 we give an overview of the biharmonic boundary integral method and in Section 2.3 we present the boundary conditions for both free and no-slip surfaces in terms of the current function ψ and vorticity ω. The technique used to obtain the instantaneous flow field and the new contour shape is described in Section 2.4 and the code validation is presented in Section 3. In Section 4 we study the blob spreading and finally in Section 5 we summarize and discuss the results.

2. FORMULATION OF THE METHOD

2.1. Basic equations and boundary conditions

For incompressible and very viscous flows, i.e. Reynolds number tending to zero, the equation of motion reduces to the so-called Stokes equation, namely

$$\overline{\nabla} p = \mu \nabla^2 \overline{v} + \rho \overline{g} = \mu \overline{\nabla} \times \overline{\omega} + \rho \overline{g}, \tag{1}$$

where p is the pressure, $\overline{v}$ is the velocity vector, μ is the viscosity and g is gravity. Also, we define the (minus) vorticity $\overline{\omega} = -\overline{\nabla} \times \overline{v}$ and use the incompressibility condition

$$\overline{\nabla} \cdot \overline{v} = 0. \tag{2}$$

We consider a fluid bounded by both free surfaces and no-slip rigid surfaces. At the free surfaces both the normal and tangential stresses are equal to zero, as the interaction with a virtual external fluid is neglected. The resulting boundary conditions are

$$\sigma_{ij} n_i t_j = 0 \quad \text{and} \quad \sigma_{ij} n_i n_j = 0, \quad i, j = 1, 2, \tag{3}$$

where n_i is the outward normal, t_i is the tangent unit vector oriented counter-clockwise and σ_{ij} is the stress tensor given by

$$\sigma_{ij} = -p\delta_{ij} + \mu \left(\frac{\partial v_i}{\partial x_j} + \frac{\partial v_j}{\partial x_i} \right). \tag{4}$$

At the no-slip rigid surfaces both the normal and tangential components of velocity are zero, i.e.

$$v_t = v_n = 0. \tag{5}$$

Now we limit ourselves to a fully two-dimensional plane geometry with horizontal and vertical co-ordinates x and y respectively. The components of v may be written in terms of the streamfunction ψ as (see (2))

$$v_x = \frac{\partial \psi}{\partial y}, \qquad v_y = -\frac{\partial \psi}{\partial x}, \tag{6}$$

so that Stokes equation (1) takes the well-known form[21]

$$\nabla^2 \psi = \omega, \qquad \nabla^2 \omega = 0. \tag{7}$$

In consequence, the problem reduces to finding the functions $\psi(x, y)$ and $\omega(x, y)$ within the domain containing the fluid (whose shape is supposed to be known) under the above boundary conditions conveniently expressed in terms of ψ and ω (see next subsection). The velocity and pressure field can later be obtained from (6) and (1) respectively. Note that as the time τ does not occur explicitly in the equations, the time evolution of the flow is determined by the deformation of the free contour resulting from the instantaneous velocity field, which in turn depends only on the instantaneous contour shape (and not on its rate of change).

2.2. *Biharmonic boundary integral method*

As (7) is the split form of the biharmonic equation $\nabla^4\psi = 0$, we solve it by using the biharmonic boundary integral method.[14,16] Green's theorem for a domain Ω enclosed by a boundary $\partial\Omega$ allows us to express ψ and ω at an arbitrary point $p \in \Omega + \partial\Omega$ in the form

$$\eta(p)\psi(p) = \oint_{\partial\Omega}\left(\psi(q)\frac{\partial G_1(p,q)}{\partial n} - \frac{\partial\psi(q)}{\partial n}G_1(p,q)\right)\mathrm{d}q + \frac{1}{4}\oint_{\partial\Omega}\left(\omega(q)\frac{\partial G_2(p,q)}{\partial n} - \frac{\partial\omega(q)}{\partial n}G_2(p,q)\right)\mathrm{d}q,$$

$$\eta(p)\omega(p) = \oint_{\partial\Omega}\left(\omega(q)\frac{\partial G_1(p,q)}{\partial n} - \frac{\partial\omega(q)}{\partial n}G_1(p,q)\right)\mathrm{d}q, \tag{8}$$

where $q \in \partial\Omega$ and $\eta(p)$ is given by[14]

$$\eta(p) = \begin{cases} 0, & p \notin \Omega + \partial\Omega, \\ \varphi, & p \in \partial\Omega, \\ 2\pi, & p \in \Omega. \end{cases} \tag{9}$$

Here, φ is the internal angle (in radians) between the tangents to $\partial\Omega$ on both sides of $p \in \partial\Omega$. The Green functions G_1 and G_2 are[16]

$$G_1 = \log|p-q|, \qquad G_2 = |p-q|^2(\log|p-q| - 1). \tag{10}$$

The governing integral equations (8) over the boundary $\partial\Omega$ can be discretized by assuming that the boundary is formed by a succession of straight segments where the functions ψ, $\partial\psi/\partial n$, ω and $\partial\omega/\partial n$ may be taken as constants (Figure 1). Thus, following Kelmanson,[16] the discretized form of (8) can be represented by

$$\mathbf{A}\boldsymbol{\psi} + \mathbf{B}\boldsymbol{\psi}' + \mathbf{C}\boldsymbol{\omega} + \mathbf{D}\boldsymbol{\omega}' = \mathbf{0}, \qquad \mathbf{A}\boldsymbol{\omega} + \mathbf{B}\boldsymbol{\omega}' = \mathbf{0}, \tag{11}$$

where $\mathbf{A}$, $\mathbf{B}$, $\mathbf{C}$ and $\mathbf{D}$ are $m \times m$ matrices and $\boldsymbol{\psi}$, $\boldsymbol{\psi}'$, $\boldsymbol{\omega}$ and $\boldsymbol{\omega}'$ are the vectorized values of ψ, $\partial\psi/\partial n$, ω and $\partial\omega/\partial n$ at the middle of the segments respectively. The polygonally discretized boundary $\partial\Omega$ yields analytical expressions for the elements of these matrices.[14,16] In addition to the algebraic system (11) of $2m$ equations and $4m$ unknowns, there is a set of $2m$ equations resulting from the boundary conditions.

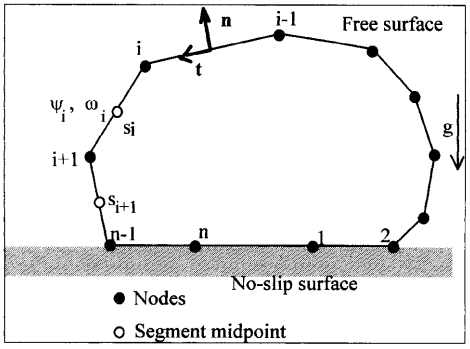

Figure 1. Representation of contour by a polygon. All the variables are defined at the segment midpoints

2.3. Boundary conditions in terms of ψ and ω

Equation (6) may be conveniently written in terms of the normal and tangential directions as

$$v_n = \frac{\partial \psi}{\partial t}, \qquad v_t = -\frac{\partial \psi}{\partial n}, \tag{12}$$

whence the boundary condition (5) on a rigid no-slip surface may be satisfied by requiring

$$\frac{\partial \psi}{\partial n} = 0, \qquad \psi = \text{const.} \tag{13}$$

along this portion of the boundary.

Analogously, at a free surface the zero-tangential-stress boundary condition given by (3) may be expressed as

$$\sigma_{ij} n_i t_j = \mu\left(\frac{\partial v_n}{\partial t} + \frac{\partial v_t}{\partial n}\right) = 0, \tag{14}$$

so that in terms of ψ we have

$$\frac{\partial^2 \psi}{\partial t^2} - \frac{\partial^2 \psi}{\partial n^2} = 0. \tag{15}$$

Hence the vorticity at the contour is

$$\omega = \nabla^2 \psi = \frac{\partial^2 \psi}{\partial t^2} + \frac{\partial^2 \psi}{\partial n^2} = 2\frac{\partial^2 \psi}{\partial t^2}. \tag{16}$$

As in the numerical calculation the values of ψ, ω, etc. are defined only on the contour, it is convenient to express the derivatives with respect to the tangent direction t in terms of derivatives with respect to the contour arc length s. Thus $\partial/\partial t$ coincides with $\partial/\partial s$ and[22,23]

$$\frac{\partial^2 \psi}{\partial t^2} = \frac{\partial^2 \psi}{\partial s^2} + \kappa \frac{\partial \psi}{\partial n}, \tag{17}$$

where $\kappa = \mathrm{d}\phi/\mathrm{d}s$ is the local curvature of the free surface, with ϕ the angle between the x-axis and the tangential unit vector t. Here κ is positive if the centre of curvature is within the fluid region. The zero-tangential-stress condition (15) is then written as

$$-\omega + 2\frac{\partial^2 \psi}{\partial s^2} + 2\kappa \frac{\partial \psi}{\partial n} = 0. \tag{18}$$

On the other hand, the condition on the normal stress given by (3) takes the form

$$-p + 2\mu \frac{\partial v_n}{\partial n} = 0. \tag{19}$$

Then, using (12) and the identity[22]

$$\frac{\partial^2 \psi}{\partial t \partial n} = \frac{\partial^2 \psi}{\partial s \partial n} - \kappa \frac{\partial \psi}{\partial s}, \tag{20}$$

we have

$$-p + 2\mu\left(\frac{\partial^2 \psi}{\partial s \partial n} - \kappa \frac{\partial \psi}{\partial s}\right) = 0. \tag{21}$$

Note that this boundary condition involves not only ψ and ω but also the pressure p. By using the tangential component of the Stokes equation (1), this quantity may be expressed in terms of ψ and ω as

$$\frac{\partial p}{\partial t} = \overline{\nabla} p \cdot \bar{t} = -\mu \frac{\partial \omega}{\partial n} - \rho g t_y, \tag{22}$$

where t_y is the y-component of the tangent unit vector. Thus by deriving (21) with respect to s, eliminating $\partial p/\partial s$ $(= \partial p/\partial t)$ through (22) and using (20), we get

$$\frac{\partial \omega}{\partial n} + 2\frac{\partial^2}{\partial s^2}\frac{\partial \psi}{\partial n} - 2\frac{\partial}{\partial s}\left(\kappa \frac{\partial \psi}{\partial s}\right) = -\frac{\rho g}{\mu} t_y. \tag{23}$$

A similar expression (without gravity but with capillarity) has also been used by Kuiken.[20] In summary, the boundary conditions for a free surface in terms of ψ, $\partial\psi/\partial n$, ω, $\partial\omega/\partial n$ and their derivatives with respect to s are given by (18) and (23).

The third and fourth sets of m equations needed to complete the algebraic system of (11) may now be constructed by combining simultaneously the conditions at both the no-slip surface and the free surface. In fact, the third set is the discretized form of both (13) and (18):

$$\mathbf{R}\boldsymbol{\psi} + \mathbf{S}\boldsymbol{\psi}' + \mathbf{T}\boldsymbol{\omega} = \mathbf{0}, \tag{24}$$

where $\mathbf{R}$, $\mathbf{S}$ and $\mathbf{T}$ are $m \times m$ matrices. For the ith segment at a no-slip surface we have $S_{ij} = \delta_{ij}$ and $R_{ij} = T_{ij} = 0$, while at a free surface $\mathbf{R}$ is a tridiagonal matrix containing the centred second-order derivative operator on the arc length s, $S_{ij} = \kappa\delta_{ij}$ and $T_{ij} = -\delta_{ij}$.

Analogously, the fourth set of m equations is obtained from (13) and (23). The corresponding algebraic system is

$$\mathbf{U}\boldsymbol{\psi} + \mathbf{V}\boldsymbol{\psi}' + \mathbf{W}\boldsymbol{\omega}' = \mathbf{b}, \tag{25}$$

where $\mathbf{U}$, $\mathbf{V}$ and $\mathbf{W}$ are $m \times m$ matrices and $\mathbf{b}$ is a vector. The condition $\psi = 0$ at the ith segment of a no-slip surface requires $U_{ij} = \delta_{ij}$, $V_{ij} = W_{ij} = 0$ and $b_i = 0$. On a free surface the elements of $\mathbf{U}$, $\mathbf{V}$ and $\mathbf{W}$ contain the centred second-order discretized derivative operators of (23), with

$$b_i = \left[-\frac{\rho g}{\mu} t_y\right]_i. \tag{26}$$

2.4. Calculation of instantaneous flow and time evolution of contour

The key step in the solution of an unsteady problem is the determination of the instantaneous flow for a given contour and boundary conditions. Here this is done by solving simultaneously the governing equations (11) and the corresponding boundary conditions (24) and (25) in the vector form $(4m \times 4m)$

$$\begin{pmatrix} \mathbf{A} & \mathbf{B} & \mathbf{C} & \mathbf{D} \\ \mathbf{0} & \mathbf{0} & \mathbf{A} & \mathbf{B} \\ \mathbf{R} & \mathbf{S} & \mathbf{T} & \mathbf{0} \\ \mathbf{U} & \mathbf{V} & \mathbf{0} & \mathbf{W} \end{pmatrix} \cdot \begin{pmatrix} \boldsymbol{\psi} \\ \boldsymbol{\psi}' \\ \boldsymbol{\omega} \\ \boldsymbol{\omega}' \end{pmatrix} = \begin{pmatrix} 0 \\ 0 \\ 0 \\ b \end{pmatrix}, \tag{27}$$

where the matrices $\mathbf{A}$, $\mathbf{B}$, $\mathbf{C}$ and $\mathbf{D}$ are dense and $\mathbf{R}$, $\mathbf{S}$, $\mathbf{T}$, $\mathbf{U}$, $\mathbf{V}$ and $\mathbf{W}$ are sparse. We observe that in general this matrix is ill-conditioned for conventional iterative algorithms, so we solved it by an LU decomposition.

In the problems with mirror symmetry with respect to the x-co-ordinate we only solve the half-space $x > 0$, i.e. the calculation is limited to $m/2$ segments. In this case the coefficients of the $(m/2) \times (m/2)$ matrices **A**, **B**, **C** and **D** must be modified taking into account that $\psi(-x, y) = -\psi(x, y)$ and $\omega(-x, y) = -\omega(x, y)$ in the Green integrals of (8). The coefficients of the $(m/2) \times (m/2)$ matrices **R**, **S**, **T**, **U**, **V** and **W** are unaltered and then the matrix of (27) is reduced to $2m \times 2m$.

Once (27) is solved, the Green integrals of (8) give ψ and ω within the fluid region in terms of the values of ψ, $\partial\psi/\partial n$, ω and $\partial\omega/\partial n$ at the contour. To obtain the time evolution of the contour, the nodes are moved according to their corresponding velocities with the Euler approximation

$$x(\tau + \Delta\tau) = x(\tau) + v_x \Delta\tau, \qquad y(\tau + \Delta\tau) = y(\tau) + v_y \Delta\tau, \tag{28}$$

where τ is the time and v_x and v_y are calculated from ψ and $\partial\psi/\partial n$ with second-order approximation.

Usually, after several time steps the distribution of the nodes becomes inadequate to properly discretize the contour, because of the piling of nodes and the appearance of abrupt variations in the segment lengths. This requires a reallocation of the nodes, which is done by fitting a cubic spline of the advanced contour; as a consequence, the number of nodes may then differ from one time step to another. The length of the segments is made to vary linearly along the contour from a minimum Δs_0 to a maximum Δs_q. We find empirically that when the length of a segment is such that $\Delta s \cdot \kappa > 0{\cdot}6$, the solution becomes inconsistent, so that the shorter segments must be allocated in the regions of high curvature (κ is calculated by a second-order approximation of $\mathrm{d}\theta/\mathrm{d}s$, with θ the angle of the adjacent segments with respect to the positive x-axis).

In summary, we obtain the time evolution of the contour by iterating the following procedure: matrix building, boundary value calculation, node advancing, spline fitting and contour regridling. In practice, this scheme is stable provided that each node is advanced a small fraction (typically less than 0·3) of the adjacent segment length; however, we find it convenient to reduce this fraction by an order of magnitude.

3. VALIDATION OF THE CODE

3.1. Instantaneous velocity field: Flow in a corner

The calculation of the instantaneous velocity field is validated by comparison with the velocity field provided by an exact analytic solution for the flow in a corner of angle α limited by a plane rigid boundary and a plane free boundary (Figure 2). It is well known that this problem admits separated solutions in polar co-ordinates (r, θ) of the form[16,24]

$$\psi(r, \theta) = r^{\lambda+1} f(\theta), \tag{29}$$

where λ is a real or complex constant and

$$f = A_1 \cos[(\lambda + 1)\theta] + A_2 \sin[(\lambda + 1)\theta] + A_3 \cos[(\lambda - 1)\theta] + A_4 \sin[(\lambda - 1)\theta], \tag{30}$$

with A_1, A_2, A_3 and A_4 constants to be determined.

The boundary conditions (13) for $\theta = 0$ and (18) for $\theta = \alpha$ give

$$f(0) = f'(0) = 0, \tag{31}$$

$$f''(\alpha) - f(\alpha)(\lambda^2 - 1) = 0. \tag{32}$$

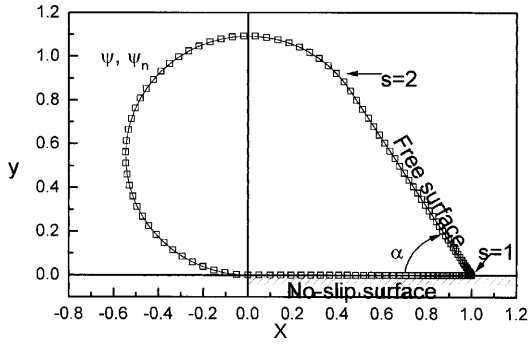

Figure 2. Grid employed to calculate flow within a corner. The no-slip surface extends from $s=0$ to 1 and the free surface from $s=1$ to 2. The values of ψ and $\partial\psi/\partial n$ from (29) are imposed on the circular arc from $s=2$ to the end

These conditions determine A_2, A_3 and A_4 in terms of A_1 as

$$A_2 = \frac{A_1}{\lambda+1}\frac{(\lambda+1)\cos[(\lambda+1)\alpha]-(\lambda-1)\cos[(\lambda-1)\alpha]}{\sin[(\lambda-1)\alpha]-\sin[(\lambda+1)\alpha]},$$
$$A_3 = -A_1, \qquad A_4 = -\frac{\lambda+1}{\lambda-1}A_2, \tag{33}$$

where A_1 may be arbitrarily fixed since it determines merely the magnitude of the velocity field. On the other hand, the condition on the normal stress given by (23) leads to

$$f'''(\alpha) + (3\lambda^2+1)f'(\alpha) = -\frac{\rho g}{\mu}\frac{\sin\alpha}{r^{\lambda-2}}. \tag{34}$$

This equation determines $\lambda(\alpha)$ only if the right-hand side is negligible. Thus the *ansatz* of (29) represents the flow within the corner for $g \to 0$ or else for $r \to 0$ with $\lambda < 2$. If one of these assumptions holds, $\lambda(\alpha)$ is a real monotonically decreasing function in the range $0{\cdot}37 < \alpha < 1{\cdot}367$ rad ($2 > \lambda > 0{\cdot}646$); for larger angles, complex roots of (34) are also possible. For $\alpha > \pi/4$ we have $\lambda < 1$ and then the vorticity

$$\omega = r^{\lambda-1}[(\lambda+1)^2 f + f''] \tag{35}$$

diverges for $r \to 0$. It should be noted that neither the force exerted on the solid nor the viscous dissipation rate diverges in this case, as happens in the steady state solution by Huh and Scriven.[25]

We calculate this flow for the case $\alpha = 1$ rad ($\lambda = 0{\cdot}814\ldots$). To do this, we construct a closed contour by smoothly connecting the sides of the corner with an arc of a circle (see Figure 2), where we impose the values of ψ and $\partial\psi/\partial n$ corresponding to the theoretical solution. We adopt a minimum segment length $\Delta s_0 = 0{\cdot}001$ at $r=0$ and a maximum $\Delta s_q = 0{\cdot}05$ at the joint with the arc, which in turn has been uniformly discretized. In Figure 3 we show a comparison between the numerical results (symbols) and the exact analytical solution (lines) as a function of s near the apex ($s=1$). A remarkable observation is that ω and $\partial\omega/\partial n$ are well described by the numerical solution close to the apex, where they diverge (see Figure 3(b)). In other words, there is no need for any special treatment (such as the incorporation of the analytical nature of the singularity into the method[14,16]) of the apex region other than a suitable discretization. In conclusion, the numerical code describes properly the instantaneous velocity field and its derivatives in corners limited by free and no-slip surfaces, even in the presence of vorticity singularities.

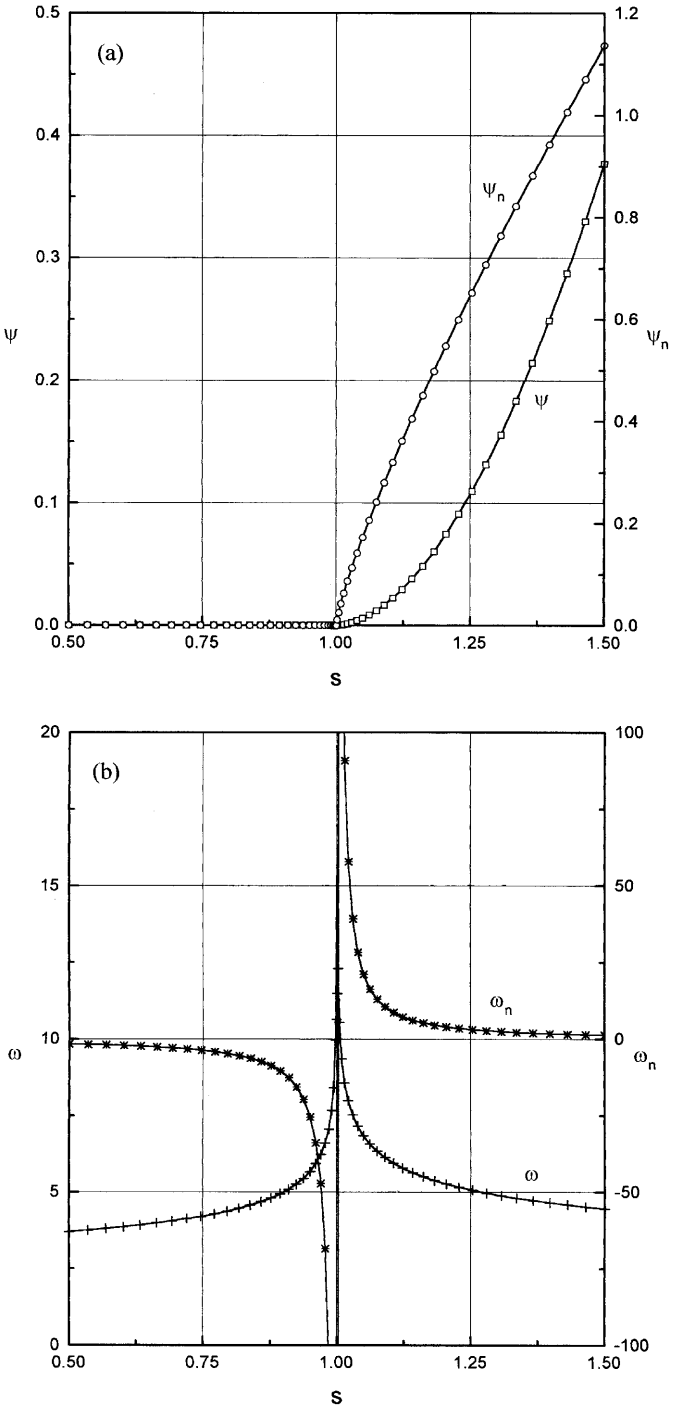

Figure 3. Comparison between analytical solution (full lines) and numerical results (symbols) for test problem of Figure 2 near apex: (a) ψ and $\partial\psi/\partial n$ and (b) ω and $\partial\omega/\partial n$ obtained with $\Delta s_0 = 0{\cdot}001$ and $\Delta s_q = 0{\cdot}05$

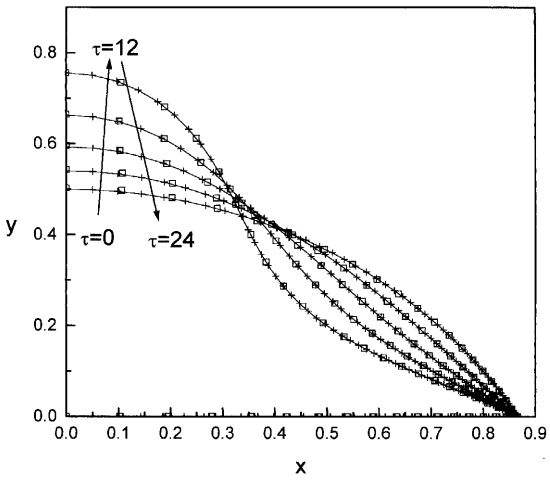

Figure 4. Contour evolution of a hanging blob. Initially it has the shape of a truncated cylinder of unity radius and height 0·5 and $g=-1$. The contours for $\tau=0$, 3, 6, 9, 12 are plotted with crosses ($\Delta s_0=0{\cdot}005$, $\Delta s_q=0{\cdot}05$), while the reversed flow ($g=1$) is represented with squares for $\tau=15$, 18, 21, 24 ($\Delta s_0=0{\cdot}01$, $\Delta s_q=0{\cdot}1$)

3.2. Time evolution: Reversibility of flow

In order to test the accuracy of the evolutionary part of the code, we should compare the numerical results with the exact analytical unsteady solution of a problem with both free and no-slip surfaces. Unfortunately, we do not have such a solution at hand and so we resort to the well-known time reversibility property of Stokes flows. In particular, we wish to show that the code is able to give practically identical time evolutions for different discretizations.

In Figure 4 we show the contour evolution under gravity of a cylindrical hanging blob ($g=-1$). We start the calculation with a truncated cylinder of unity radius and height 0·5 upon a substrate; we use $\Delta s_0=0{\cdot}005$ at the contact line and $\Delta s_q=0{\cdot}05$ at the centre of symmetry. The simulation was stopped at $\tau=12$ (crosses); then, by taking the contour at $\tau=12$ as the initial condition, we let the code run until $\tau=24$ with $g=1$ (circles). For this second flow we change to a coarse grid with $\Delta s_0=0{\cdot}01$ and $\Delta s_q=0{\cdot}1$. The coincidence between the profiles with $g=-1$ at $\tau=0$, 3, 6, 9, 12 and those obtained with $g=1$ at $\tau=15$, 18, 21, 24 respectively is representative of the code's ability to describe properly the evolution of the flow.

4. SPREADING OF A BLOB UNDER GRAVITY ON A NO-SLIP SURFACE

Consider an initial fluid configuration in the form of an infinitely long cylinder lying on a horizontal rigid surface (substrate). The fluid is supposed to spread on the substrate only due to gravity, as in the first stage of the experiments quoted in Section 1.[13] In Figure 5 we show the evolution of the contour for three different initial shapes of equal area σ: (a) a truncated circular cross-section of unity radius and height 1·9, (b) a truncated ellipse (axis ratio 1·5) with its major axis in the vertical direction and (c) a square with rounded corners; we use $\rho=\mu=g=1$, $\Sigma=3{\cdot}08$ and a discretization with $\Delta s_0=0{\cdot}008$ and $\Delta s_q=0{\cdot}08$ (all quantities are in arbitrary units). During the calculation the area σ remains constant within 0·05 per cent. Each calculation of the instantaneous velocity field on a PC 80486 at 50 MHz takes about 20 s; a complete evolution as shown in Figure 5 takes around 15 h, starting with about 150 nodes and finishing with about 300. A noteworthy effect is displayed in case (c), consisting of a remanence of high-curvature regions related to the initial corners. This affect

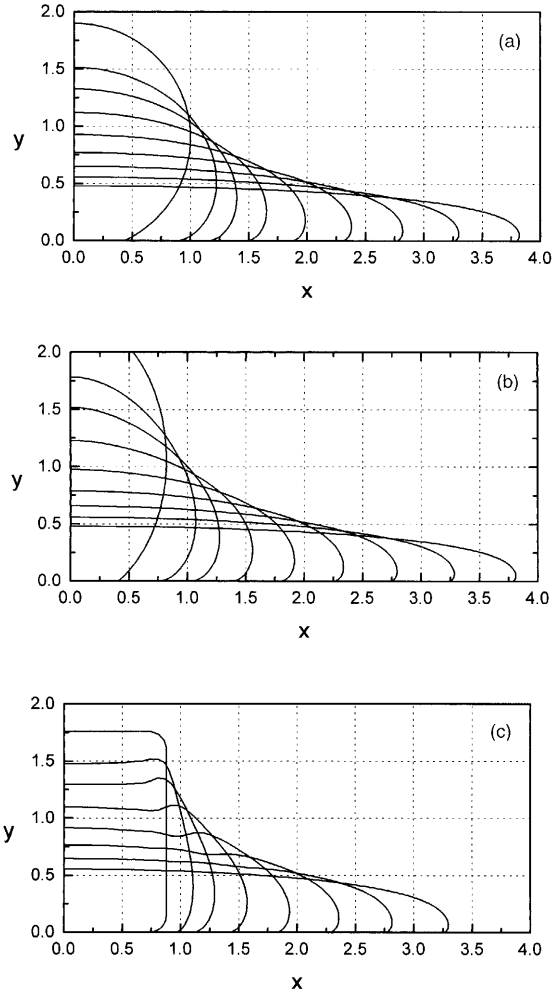

Figure 5. Height profiles for blob spreading driven by gravity of different intial shapes of equal area: (a) circle truncated at its base, (b) ellipse (axis ratio 1·5) with its major axis in vertical direction and truncated at its base; (c) square with rounded corners. The profiles are shown in the order $\tau = 0$, 1, 2, 4, 8, 16, 32, 64, 128

cannot be ascribed to a numerical origin and is certainly due to the physical properties of the flow near a free corner.

As the flow proceeds, the current head adopts in all cases a rounded shape characterized by the ratio between the thickness h^* at x_{cl} and the width $\Delta x = x_f - x_{cl}$. Here x_f is the position of the leading nose and x_{cl} is the projection of the contact line between the free contour and the substrate. A noticeable fact that has been observed in experiments is that the aspect ratio $h^*/\Delta x$ asymptotically reaches a value close to four; this result is numerically reproduced as shown in Figure 6, where the evolution of $h^*/\Delta x$ is plotted versus the flatness ratio h_0/x_f (h_0 is the height at $x = 0$) for the three cases of Figure 5. The asymptotic geometrical similarity of the current head may be visualized by scaling the co-ordinates x and y with h^*; in fact, this leads to a coincidence of the numerical profiles in the head region. In Figure 7 we compare an asymptotic numerical profile with the experimental profiles[13] obtained for an axisymmetric blob of silicone oil with viscosity $v = \mu/\rho = 1274{\cdot}7$ cm^2 s^{-1}

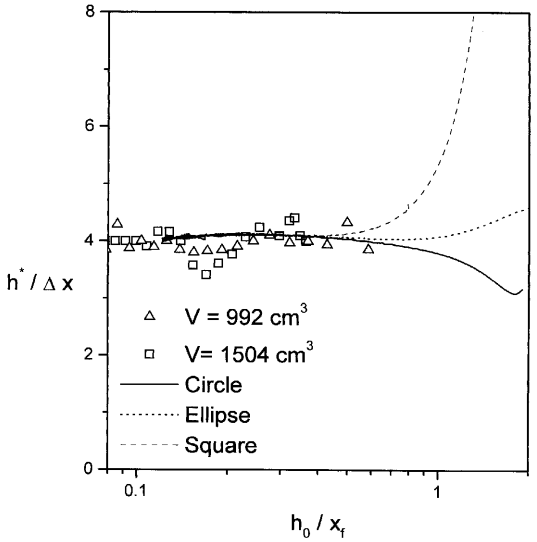

Figure 6. Time evolution of aspect ratio $h^*/\Delta x$ of current head for cases of Figure 5. The symbols correspond to experimental data from axisymmetric spreadings of silicone oil[13]

and volume $V = 1504$ cm^3; the extension of the spreading was $13 < x_f < 23$ cm and h^* ranged from 1·35 to 0·25 cm. As $\Delta x < 0{\cdot}02x_f$, the flow near the current head may safely be assumed as plane in a first approximation. Note that the general agreement is very good, except for the profile of triangles which corresponds to $h^* = 0{\cdot}25$ cm $= 1{\cdot}67a$ and, in consequence, may be affected by surface tension.[13]

A scaling law for h^* may be easily obtained from dimensional analysis; in fact, if we take ρ, μ, g and the front velocity v_f as the aracteristic parameters of the current head, we get

$$h^* \propto \sqrt{\left(\frac{\mu v_f}{\rho g}\right)}. \tag{36}$$

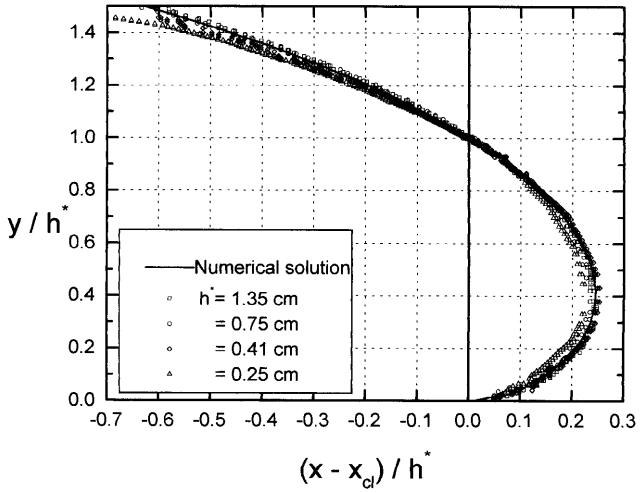

Figure 7. Comparison of an advanced numerical profile with experimental profiles measured for an axisymmetric blob[13] by using silicone oils. The symbols correspond to $h^* = 0{\cdot}25$, 0·41, 0·75, 1·35 cm for a spreading of $V = 1504$ cm^3

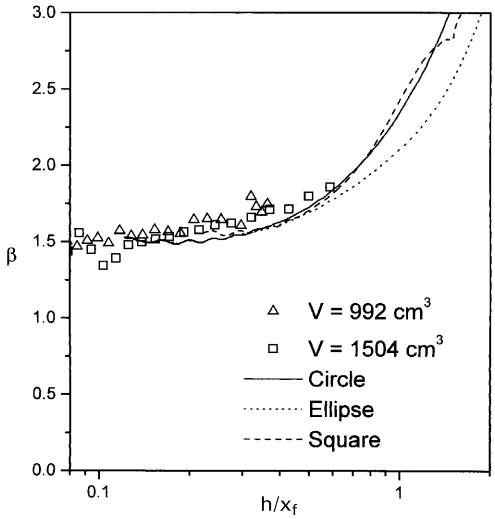

Figure 8. Ratio $\beta = h^*/\sqrt{(\mu v_f/\rho g)}$ versus flatness ratio h_0/x_f for cases of Figure 5 and comparison with experimental data[13] (symbols)

This relationship may be interpreted in terms of a balance between the weight of the head and the vertical viscous force generated by the flow, as they are respectively proportional to $\rho g h^{*2}$ and μv_f. In Figure 8 the ratio $\beta = h^*/\sqrt{(\mu v_f/\rho g)}$ is plotted versus h_0/x_f for the three cases of Figure 5; as the spreading develops, β tends to a constant near 1·5, in agreement with the experimental data* for an axisymmetric blob. As a result, the aspect ratio $h^*/\Delta x$ (≈ 4) and β ($\approx 1{\cdot}5$) are independent of the initial conditions, i.e. these quantities may be considered as representative of local properties of the current head.

In order to give a more detailed description of the (asymptotic) head shape, we plot the angle ϕ (defined as the angle between the tangent to the contour and the positive x-axis) and the curvature κ as functions of the arc length $s - x_{cl}$ (Figure 9). Note that κ increases apparently without bound as $s \to x_{cl}$, following approximately a logarithmic divergence. In spite of this divergence, ϕ is a continuous function of s, insuring a smooth connection between the free surface and the substrate.

Owing to the geometrical similarity, not only the shape but also the velocities of the contour in the vicinity of the contact line reduce to universal curves when divided by v_f; in Figure 10 we plot v_x/v_f and v_y/v_f along the contour. Note that v_g has a minimum at the nose of the head (about $0{\cdot}45h^*$ from the contact line) and that v_x has a broad maximum near $1{\cdot}89h^*$ from x_{cl}. A noticeable result is that ω has a singular behavior in this region (see Figure 11). The divergence of both ω and κ is probably due to the sudden discontinuity in the boundary conditions at the contact line. Likewise, a divergence on $\partial\omega/\partial n$ is also found there, together with some numerical oscillations on a few nodes. These singularities might adversely affect the rate of convergence of the method for $\Delta s_0 \to 0$. A convergence test is depicted in Figure 11, where $\omega(s)$ curves are plotted for different values of Δs_0 (at the contact line) and Δs_q (at the centre of symmetry). Clearly, except for a region close to the contact line, the $\omega(s)$ curves are practically coincident.

In Figures 12(a) and 12(b) we plot the streamlines in the laboratory frame and in a reference system moving with the leading nose velocity v_f respectively. The curling of the streamlines in the

* This value is not explicitly given in Reference 13 but may be calculated from the reported figures.

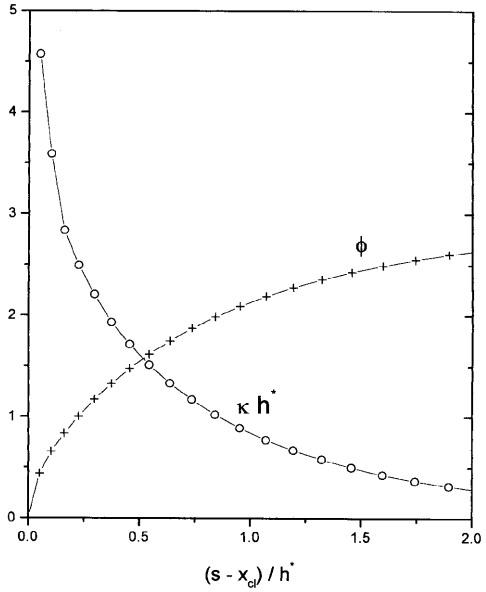

Figure 9. Angle ϕ and dimensionless curvature κh^* versus $(s - x_{cl})/h^*$ along free surface, showing continuity of ϕ and divergence κ at contact line

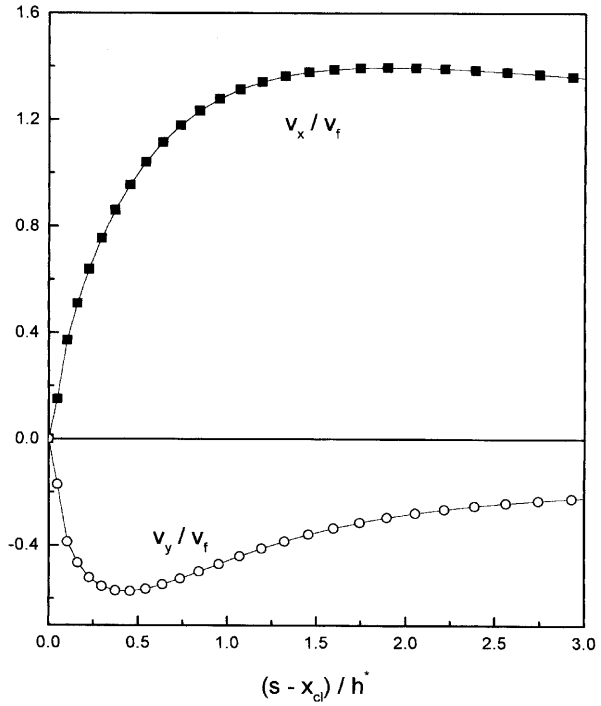

Figure 10. Velocities along free surface in units of nose velocity v_f

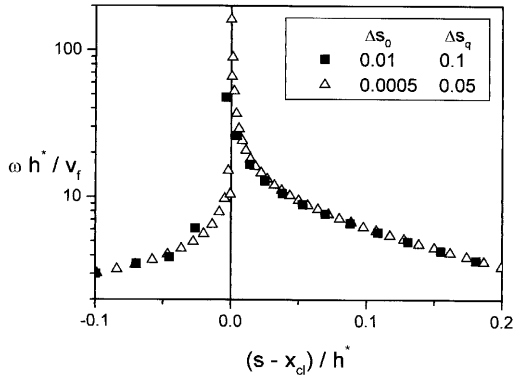

Figure 11. Convergence test: calculated $\omega(s)$ curves for different values of Δs_0 and Δs_q near contact line

head region is evident, especially in the second representation. The equivorticity lines are plotted in Figure 12(c); the high concentration of lines at the contact line is due to the divergence of ω.

As concerns the global properties of the flow, it must be noticed that the lubrication approximation may be applied as $h_0/x_f \to 0$. In this limit the height profile tends to[5,6]

$$\frac{h(x)}{h_0} = \left[1 - \left(\frac{x}{x_f}\right)^2\right]^{1/3} \tag{37}$$

(which holds for both plane and axial geometries).

To show the convergence of the two-dimensional flow to this one-dimensional limit, we present in Figure 13 plots of h/h_0 versus x/x_f for different values of the flatness ratio h_0/x_f, together with the 1D profile given by (37). There is always a region near the contact point where the 2D profiles differ markedly from the 1D profile. However, the size of this region decreases as the spreading advances, so that (37) is suitable for an increasing part of the flow.

According to the numerical solution, the size of this region (say, h^*) is related asymptotically to the flatness ratio as shown in Figure 14. This functional relationship is independent of the initial conditions and has the form

$$\frac{h^*}{h_0} \propto \left(\frac{h_0}{x_f}\right)^{1/2} \tag{38}$$

An analogous dependence was also found in the axisymmetric experiments,[13] as shown by the symbols reported in this figure.

It is interesting to note that the above dependence may be interpreted in terms of a simple heuristic approach. The spreading velocity consistent with (37) is

$$v_f \propto \frac{\rho g}{\mu}\frac{h_0^3}{x_f} \tag{39}$$

(this proportionality holds for both plane and axial symmetries). On the other hand, (36) relates v_f with h^*; thus, by substituting this expression into (39), we obtain the relationship of (38). Alternatively, (38) may be obtained by matching the profile given by (37) and the 2D profile at $x \approx x_f$, where $h \approx h^*$, bearing in mind the geometrical similarity of the head shape.

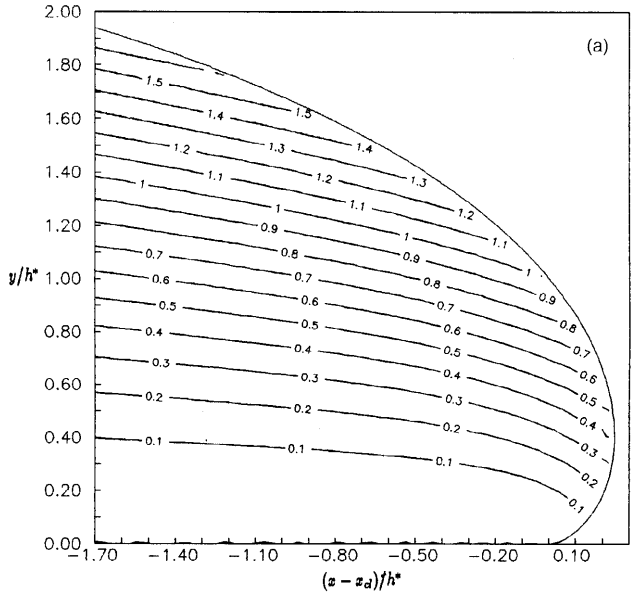

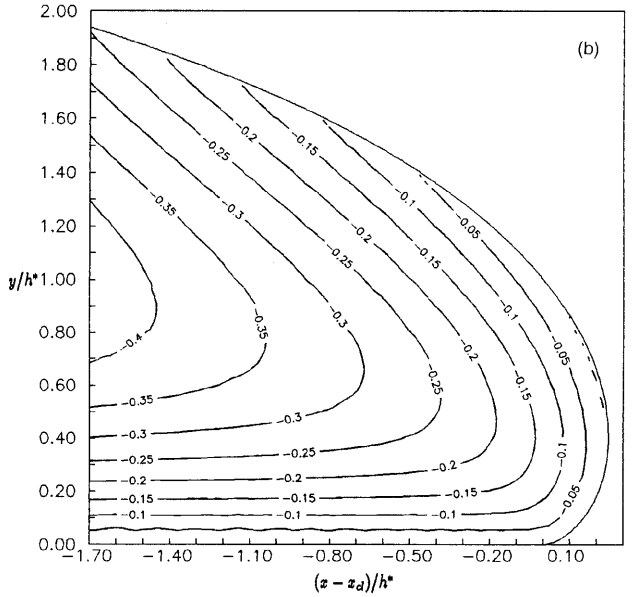

Figure 12. Current lines (a) in laboratory system of reference and (b) in frame moving with velocity v_f. (c) Equivorticity lines. The values of ψ and ω are in units of $v_f h^*$ and v_f/h^* respectively

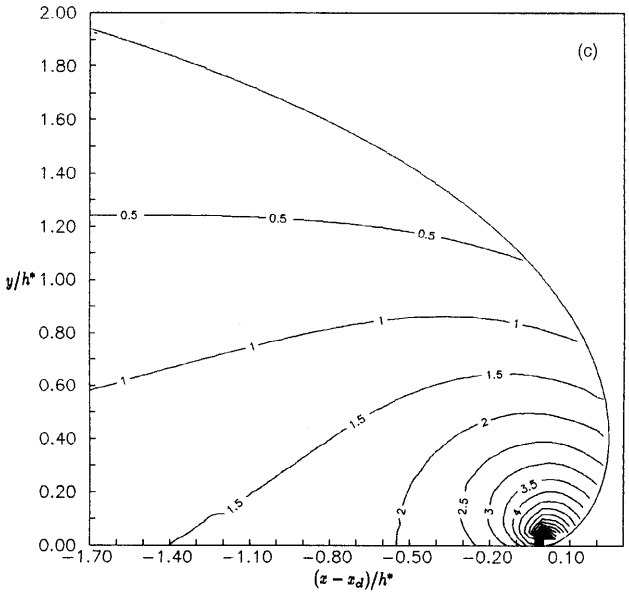

Figure 12. (*continued*)

5. CONCLUSIONS

We implement a numerical code by extending the boundary element integral method to solve unsteady Stokes flows in plane symmetry. The boundary may be spanned into sections of free and no-slip surfaces. We test the ability of the code to describe the velocity field corresponding to a given boundary configuration and the evolution of the free spans of the boundary. The first aspect is tested by comparison with the exact analytical solution for the flow in a corner region, which exhibits singularities of both ω and $\partial\omega/\partial n$. The second aspect is tested by resorting to the reversibility of Stokes flows.

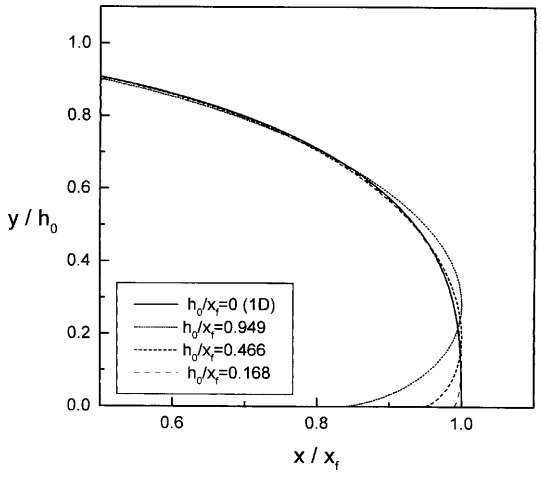

Figure 13. Dimensionless profiles showing convergence to one-dimensional solution (37) for different flatness ratios

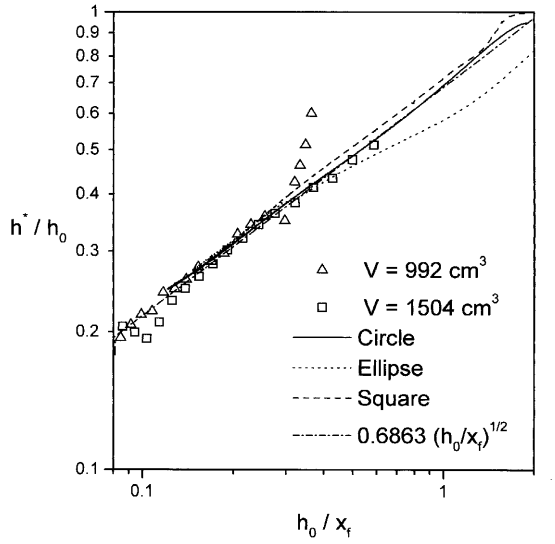

Figure 14. Ratio h^*/h_0 versus the flatness ratio h_0/x_f for cases of Figure 5 and comparison with experimental data[13] (symbols)

For the case of interest in this work, namely the viscous gravity spreading of a blob on a rigid no-slip surface, we obtain the time evolution of the two-dimensional flow. As the flatness ratio h_0/x_f reduces, the current head acquires a definite shape, so that its profile may be reduced to a universal curve when scaled with its height h^* in the directions x and y. Besides, the calculated aspect ratio of the current head, $h^*/\Delta x$, is approximately four and h^* scales with the square root of the front velocity v_f as given by (36) with a prefactor close to $\approx 1{\cdot}5$. The agreement between these results and the experiments reported elsewhere[13] for h^* larger than the capillary length a suggests that the advancing mechanism simulated by the calculation is appropriate as long as capillary effects are not relevant.

The numerical results shed some light on additional interesting features of the flow that experiments could hardly reveal, which, as far as we know, have not been reported previously. The shape of the head is given by a curve which smoothly connects the free surface with the substrate, with the noticeable property that the curvature diverges logarithmically there. Likewise, we obtain a detailed description of the streamline pattern (Figures 12(a) and 12(b)) and the vorticity distribution (Figure 12(c)); all these curves are universal near the contact line because of the geometrical similarity of the head. The vorticity distribution also diverges at the contact line.

ACKNOWLEDGEMENTS

This work was supported by the Consejo Nacional de Investigaciones Científicas y Técnicas (CONICET, Argentina), the Comisión de Investigaciones Científicas de la Provincia de Buenos Aires and the Universidad Nacional del Centro de la Provincia de Buenos Aires.

REFERENCES

1. H. E. Huppert, *J. Fluid Mech.*, **173**, 557 (1986).
2. R. C. Kerr and J. R. Lister, *Earth Planet. Sci. Lett.*, **85**, 241 (1987).
3. J. E. Simpson, *Ann. Rev. Fluid Mech.*, **14**, 213 (1982).
4. D. P. Hoult, *Ann. Rev. Fluid Mech.*, **4**, 341 (1972).
5. R. E. Pattle, *Q. J. Mech. Appl. Math.*, **12**, 407, (1959).

6. H. E. Huppert, *J. Fluid Mech.*, **121**, 43 (1982).
7. J. Gratton and F. Minotti, *J. Fluid Mech.*, **210**, 155 (1990).
8. C. Nakaya, *J. Phys. Soc. Jpn.*, **37**, 539 (1974).
9. J. E. Simpson, *J. Fluid Mech.*, **53**, 759 (1972).
10. J. W. Rotmann and J. E. Simpson, *J. Fluid Mech.*, **135**, 95 (1983).
11. J. E. Simpson and R. E. Britter, *J. Fluid Mech.*, **94**, 477 (1979).
12. N. Didden and T. Maxworthy, *J. Fluid Mech.*, **121**, 27 (1982).
13. B. Marino, L. Thomas, J. Diez and R. Gratton, *J. Colloid Interface Sci.*, **177**, 14 (1996).
14. A. Jaswon and G. T. Symm, *Integral Equation Methods in Potential Theory and Elastostatics*, Academic, New York, 1977.
15. G. Fairweather, F. J. Rizzo, D. H. Shippy and Y. S. Wu, *J. Comput. Phys.*, **31**, 96 (1979).
16. M. A. Kelmanson, *J. Comput. Phys.*, **51**, 139 (1983).
17. M. Kelmanson, *J. Eng. Math.*, **17**, 329 (1983).
18. W. Q. Lu and H. C. Chang, *J. Comput. Phys.*, **77**, 340 (1988).
19. R. Goodwin and G. M. Homsy, *Phys. Fluids A*, **3**, 515 (1991).
20. H. K. Kuiken, *J. Fluid Mech.*, **214**, 503 (1990).
21. G. Fairweather, F. J. Rizzo, D. H. Shippy and Y. S. Wu, *J. Comput. Phys.*, **31**, 96 (1979).
22. E. B. Hansen, *J. Fluid Mech.*, **178**, 243 (1987).
23. E. B. Hansen and M. A. Kelmanson, *J. Fluid Mech.*, **272**, 91 (1994).
24. H. K. Moffatt, *J. Fluid Mech.*, **18**, 1 (1964).
25. C. Huh and L. E. Scriven, *J. Colloid Interface Sci.*, **35**, 85 (1970).
26. P. R. Garabedian, *Commun. Pure Appl. Math.*, **19**, 421 (1966).
27. E. B. Dussan V, *Ann. Rev. Fluid Mech.*, **11**, 371 (1979); E. B. Dussan, V, E. Ramé and S. Garoff, *J. Fluid Mech.*, **230**, 97 (1991).

